2010

Synthesis of mesoporous r-Fe2O3 nanostructures for highly sensitive gas sensors and high capacity anode materials in lithium ion batteries

Bing Sun
University of Technology Sydney

Josip Horvat
University of Wollongong, jhorvat@uow.edu.au

Hyun-Soo Kim
Korea Electrotechnology Research Institute, Changwon

Woo-Seong Kim
Daejung Energy Materials Co., Ltd, Namdong-gu, Incheon

Jung-Ho Ahn
Andong National UniVersity, Gyungbuk , Korea

See next page for additional authors

Synthesis of Mesoporous α-Fe_2O_3 Nanostructures for Highly Sensitive Gas Sensors and High Capacity Anode Materials in Lithium Ion Batteries

Bing Sun,[†] Josip Horvat,[‡] Hyun Soo Kim,[§] Woo-Seong Kim,[#] Jungho Ahn,[¶] and Guoxiu Wang*,[†]

School of Chemistry and Forensic Science, University of Technology Sydney, Broadway, Sydney, NSW 2007, Australia, Institute for Superconducting and Electronic Materials, University of Wollongong, Wollongong, NSW 2522, Australia, Battery Research Center, Korea Electrotechnology Research Institute, Changwon 641-120, Korea, Daejung Energy Materials Co., Ltd, Namdong-gu, Incheon 405-820, Korea, and Department of Materials Engineering, Andong National University, Gyungbuk 760-749, Korea

Received: March 13, 2010; Revised Manuscript Received: September 28, 2010

Mesoporous α-Fe_2O_3 materials were prepared in large quantity by the soft template synthesis method using the triblock copolymer surfactant F127 as the template. Nitrogen adsorption−desorption isothermal measurements and transmission electron microscope observation revealed that the as-prepared mesoporous α-Fe_2O_3 nanostructures have large mesopores in a wide size range of 5−30 nm. It has been found that the Morin transition depends on thermal history of mesoporous α-Fe_2O_3, which is driven by surface anisotropy. Superparamagnetic behavior of mesoporous α-Fe_2O_3 is also associated with surface spins with blocking temperature around 50 K. When applied as gas sensors, mesoporous α-Fe_2O_3 nanostructures exhibited high gas sensitivity toward acetic acid and ethanol gas. As anodes in lithium ion cells, mesoporous α-Fe_2O_3 materials show a high specific capacity of 1360 mAh/g with excellent cycling stability and high rate capacity.

1. Introduction

As an n-type semiconductor, hematite (α-Fe_2O_3) has attracted a great deal of attention from researchers in different fields because of its nontoxicity, low cost, high stability under ambient conditions, and multiple functions. It has been intensively investigated for applications in lithium batteries,[1,2] sensors,[3] catalysts,[4] pigments,[5] and magnetic devices.[6] The performance of α-Fe_2O_3 strongly depends on the particle size, morphology, and structure. For use as anode material in the lithium ion battery, the reversibility of lithium intercalation in α-Fe_2O_3 depends strongly on the structure and particle size. Nanosize α-Fe_2O_3 exhibits better performance than microscale samples as the smaller particle size can greatly reduce the diffusion length of the lithium ions.[7,8] From the investigations on gas-sensing performance, the sensitivities of α-Fe_2O_3 nanospheres are much higher than those of microcrystalline α-Fe_2O_3 powders. The interconnected pores in the nanospheres are of benefit for the diffusion of gas and have been proved to offer more active sites for gas chemisorption.[9] There is growing interests in the preparation of nanomaterials with specially designed structures. Nanostructured α-Fe_2O_3 with one-dimensional nanowire/nanotube structures,[10,11] two-dimensional flake/film structures,[12,13] and three-dimensional hollow/porous structures[6,14] have already been synthesized by a variety of methods, such as the sol−gel method,[15,16] electrostatic spray deposition,[17] hydrothermal treatment,[18,19] and template method.[20,21]

Since the discovery of MCM-41 mesoporous silica in 1992, mesoporous materials have been developed into an important class of materials and occupy a very important position in materials science.[22] The mesopore structure can dramatically increase the surface area/volume ratio, which makes the mesoporous materials very useful in the surface-related applications. There is intense interest in preparing mesoporous transition-metal oxides because of their unique catalytic, magnetic, adsorptive, and electrochemical properties in applications as catalysts,[23] magnetic materials,[24] absorbents,[25] and energy convertion and storage materials.[26] Several mesoporous transition-metal oxides have already been synthesized, such as Co_3O_4,[27] Mn_2O_3,[24] Fe_2O_3,[28] TiO_2,[29] and V_2O_5;[30] however, it is still much more difficult to synthesize mesoporous transition-metal oxides than mesoporous silica. The materials with three-dimensional mesoporous architectures are normally obtained through template-directed methods, which can be simply classified into the hard template method and the soft template method. The hard templates (usually mesoporous silica or carbon) normally possess well-confined channels and pores, which strongly influence the structure of the resulting solid product. Soft templates are usually surfactants, long-chain polymers, and viruses, which function as structure-directing agents that assist in the assembly of reacting species.[20] Yang et al. first reported the synthesis of a series of metal oxides by employing nonionic polymer surfactants as templates, which could be easily removed by solvent extraction or thermal treatment.[31,32] The hard template methods usually involve a multistep synthesis process. Mesoporous silica or carbon must be prepared first. Then, the inorganic precursors are combined with the templates by impregnation or incorporation. The final product can be obtained by template removal after the solid species has formed through reaction, nucleation, and growth.[20] However, for the soft template methods, the templates can form by self-assembly in liquid solution and can be easily removed by solvent or calcination. Therefore, the soft template method is generally easier to be scaled up for large-scale production than the hard

* To whom correspondence should be addressed. E-mail: Guoxiu.Wang@uts.edu.au. Fax: +61-2-95141460.
[†] University of Technology Sydney.
[‡] University of Wollongong.
[§] Korea Electrotechnology Research Institute.
[#] Daejung Energy Materials Co., Ltd.
[¶] Andong National University.

10.1021/jp102286e
Published on Web 10/15/2010

template method. However, it is difficult to control the regularity, pore size, and pore structure using the soft template method. In this paper, we report the synthesis of mesoporous α-Fe_2O_3 nanostructures with large mesopores by using a soft template method in nonaqueous solution. The as-prepared mesoporous α-Fe_2O_3 materials exhibit unique magnetic properties, high gas sensitivity, and high reversible lithium storage capacity in lithium ion cells.

2. Experimental Section

2.1. Preparation of Mesoporous α-Fe_2O_3. In a typical synthesis, the triblock copolymer ($HO(CH_2CH_2O)_{106}(CH_2CH(CH_3)O)_{70}(CH_2CH_2O)_{106}H$) (F127) and iron nitrate were used as the template and inorganic source, respectively. F127 block copolymer (1 g) was dissolved in a mixture of propanol (5 g) and ethylene glycol (EG; 5 g). To this solution, 0.01 mol $Fe(NO_3)_3 \cdot 9H_2O$ was added with vigorous stirring over 2 h. The resulting sol solution was then aged in air at 40 °C for 7 days and then was gradually heated to 150 °C (1 °C/min) and was maintained at 150 °C for 24 h. Finally, the samples were further sintered at 400 °C for 5 h to remove the block copolymer surfactant (heating rate: 1 °C/min).

2.2. Structural, Optical, and Magnetic Characterization. The crystal structure and phase of the as-prepared mesoporous α-Fe_2O_3 were characterized by X-ray diffraction (XRD, GBC MMA) using Cu Kα radiation with 2θ ranging from 20° to 70°. Raman spectra were collected on a JOBIN Yvon Horiba Confocal Mico Raman spectrometer model HR 800 with 632.8 nm diode laser excitation on a 300 lines/mm grating at room temperature. The band gap energy of the as-prepared mesoporous α-Fe_2O_3 was calculated via ultraviolet−visible (UV−vis) spectroscopy on a Shimadzu UV-1700 spectrophotometer. The morphology and microstructures were characterized by transmission electron microscopy (TEM) and high-resolution TEM (HRTEM, JEOL 2011). N_2 adsorption−desorption measurements were conducted using a Quantachrome Autosorb analyzer at 77 K with the samples degassed at 120 °C overnight under vacuum before measurements. The magnetic moment of mesoporous α-Fe_2O_3 was measured with a vibrating sample magnetometer (VSM) option of a Quantum Design Physical Properties Measurement System (PPMS). The temperature dependence of the magnetic moments was measured in three different consecutive regimes: during warming after zero-field-cooling of the sample (ZFCW), during subsequent field cooling (FCC), and finally, during warming after field cooling (FCW). For the ZFCW measurements, the sample was cooled in zero field from 305 to 5 K, a magnetic field was applied, and the magnetic moment was measured in constant field as the temperature was swept to 305 K. The FCC measurements were performed by subsequently cooling the sample to 5 K without changing the field. The FCW measurements were performed during a further sweep of the temperature from 5 to 305 K without changing the field after the FCC measurement. The sweep rate of the temperature was 2 K/min. Several temperature scans were performed at different magnetic fields. Magnetic hysteresis loops were measured at selected temperatures with a sweep rate of the field of 50 Oe/s.

2.3. Gas-Sensing Measurement. Gas-sensing properties of the as-prepared mesoporous α-Fe_2O_3 were measured by a computer-controlled WS-30A gas-sensing measurement system. The schematics of the device and its operating principles are shown in Figure S-1 of the Supporting Information (SI).

2.4. Electrochemical Characterizations. To prepare the working electrode, the as-prepared mesoporous α-Fe_2O_3 powder (50 wt %), acetylene black (40 wt %), and poly(vinylidene fluoride) (PVDF, 10 wt %) were mixed in *N*-methyl-2-pyrrolidone (NMP) to form a slurry. The resultant slurry was pasted onto copper foil with a blade and was dried at 100 °C for 12 h under vacuum conditions followed by pressing at 200 kg cm^{-2}. Electrochemical measurements were carried out using two-electrode coin cells with lithium metal as the counter and reference electrode. The CR2032-type cells were assembled in an argon-filled glovebox. The electrolyte solution was 1 M $LiPF_6$ dissolved in a mixture of ethylene carbonate (EC) and dimethyl carbonate (DMC) with a volume ratio of 1:1. Cyclic voltammetry (CV) was carried out on a CHI 660C electrochemistry workstation with a scan rate of 0.1 mV s^{-1} from 0.005 to 3.0 V in a two-electrode system. The charge−discharge measurements were carried out at ambient temperature at different current densities in the voltage range from 0.005 to 3.0 V.

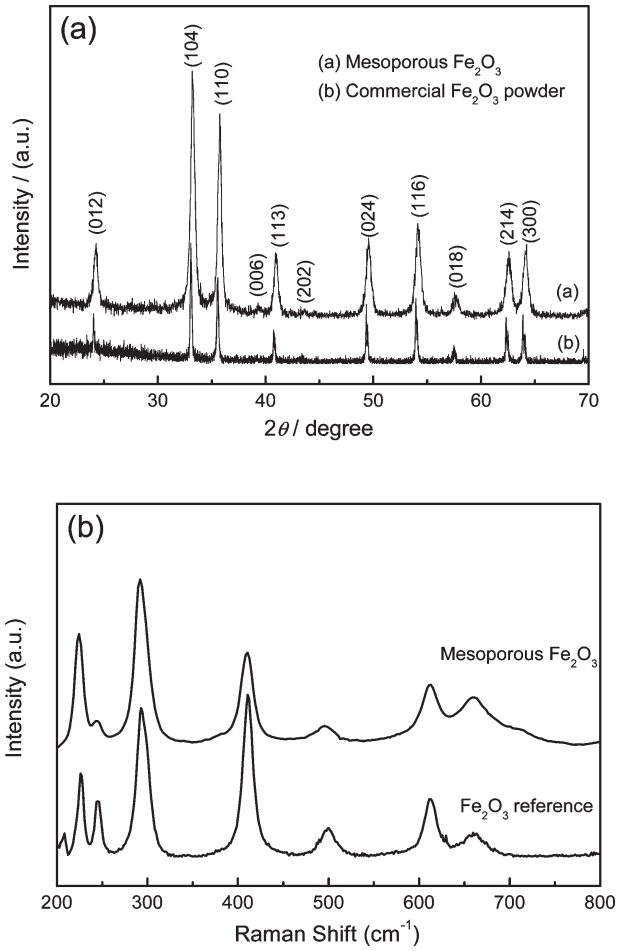

Figure 1. (a) X-ray diffraction pattern of the as-prepared mesoporous and commercial α-Fe_2O_3. (b) Raman spectrum of as-prepared mesoporous α-Fe_2O_3 and a hematite reference spectrum.

3. Results and Discussion

3.1. Structure and Morphological Analysis. Figure 1a shows the powder X-ray diffraction (XRD) pattern of the as-prepared mesoporous α-Fe_2O_3 and the commercial α-Fe_2O_3 powder (Sigma-Aldrich). All diffraction peaks can be indexed to the standard hematite (α-Fe_2O_3) crystal structure (JCPDS card number 33-0664)[10] indicating that a pure and highly crystalline product has been obtained by calcining iron oxide precursor. The average crystal size of mesoporous α-Fe_2O_3 was calculated to be about 20.6 nm on the basis of the broadening of the (104) diffraction peak using the Scherrer formula. Raman spectroscopy is a powerful tool to identify the crystal phase of Fe_2O_3. Figure

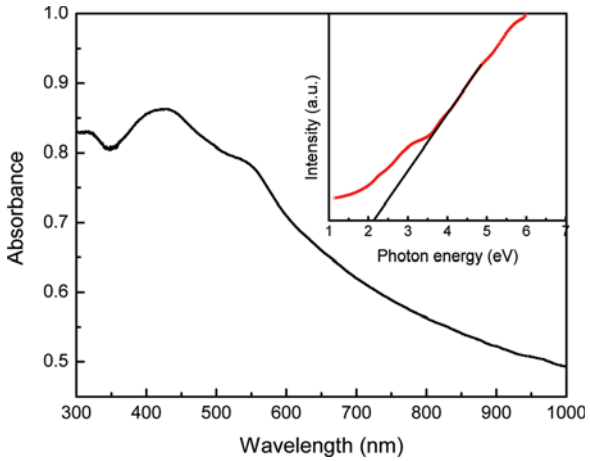

Figure 2. UV−vis spectrum of mesoporous α-Fe_2O_3.

1b shows the Raman spectrum of the as-prepared mesoporous α-Fe_2O_3 along with a hematite reference spectrum (RRUFF ID R050300).[33] The spectrum indicates a typical α-Fe_2O_3 crystal structure showing Raman peaks at 224, 292, 410, 496, and 613 cm^{-1}, which matches well with the hematite reference spectrum. Compared to the previous report on α-Fe_2O_3 microcrystalline powders, all Raman peaks of our mesoporous α-Fe_2O_3 are slightly blue-shifted.[34] This may be due to the small size of the component nanocrystals. The Raman peak around 660 cm^{-1} in the spectrum has been reported in several published papers and is attributed to a large amount of defects and local lattice disorder at the interfaces and interior faces, which leads to the reduction of space symmetry and the appearance of the new peak.[13,35] Both the XRD and Raman spectroscopy measurements confirmed the pure phase nature of mesoporous α-Fe_2O_3. The optical absorption property of the as-prepared mesoporous α-Fe_2O_3 was investigated at room temperature by UV−vis spectroscopy (Figure 2). The band gap of hematite can be calculated by the following equation:

$$(\alpha h\nu)^2 = B \times (h\nu - E_g) \quad (1)$$

where α is the absorption coefficient, $h\nu$ is the photon energy, B is a constant, and E_g is the band gap. The $(\alpha h\nu)^2$ versus $h\nu$ curve is shown as the inset in Figure 2. The band gap of the as-prepared mesoporous α-Fe_2O_3 calculated from eq 1 is 2.14 eV, which agrees well with previously reported values of 1.9−2.2 eV for n-type semiconductor α-Fe_2O_3.[36,37]

Figure 3 shows the TEM and HRTEM images of the as-prepared mesoporous α-Fe_2O_3 powders. The prepared material exhibits an ordered porous structure with different shapes of pores as shown in Figure 3a. Pores in the iron oxide materials originate from the regions previously occupied by the polymer surfactants. After the removal of the surfactant, some walls of the porous structure collapse and form a wormhole-like morphology. The selected area electron diffraction (SAED) pattern is presented in the inset of Figure 3a showing a single-crystalline-like SAED dot pattern. The HRTEM image in Figure 3b clearly presents the lattice fringes of the (110) and (102) planes of α-Fe_2O_3 corresponding to d-spacings of 0.250 and 0.388 nm. Both the HRTEM images and the SAED pattern confirm the formation of single-crystalline mesoporous α-Fe_2O_3. In addition, regular mesopore structures were extensively observed by TEM analysis, but we also found a large amount of mesoporous spheres (as shown in Figures S2 and S3 of the SI).

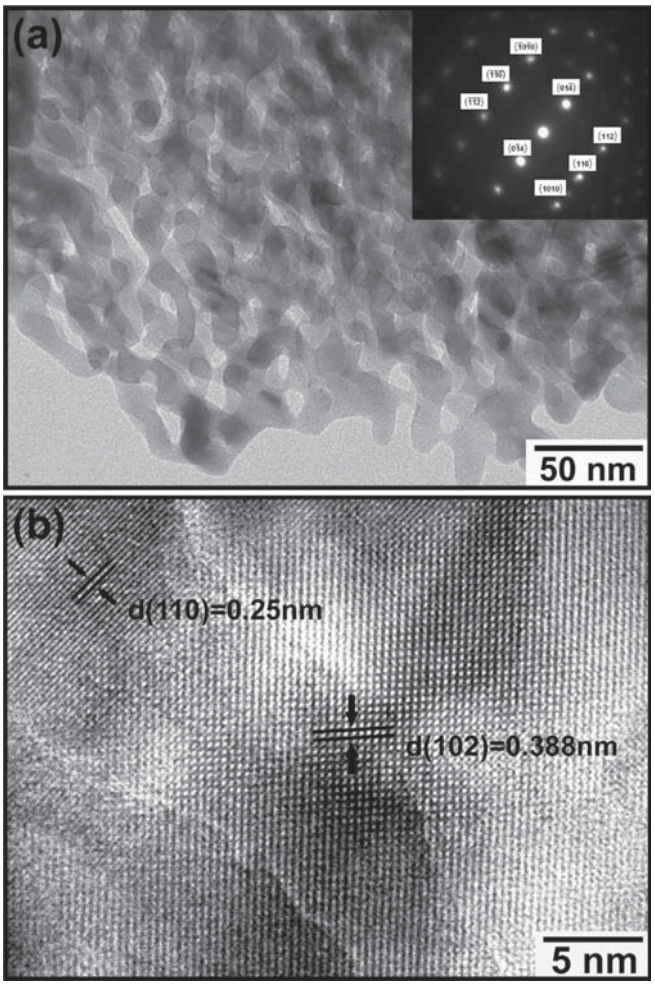

Figure 3. (a) TEM image of mesoporous α-Fe_2O_3. The inset is the corresponding selected area electron diffraction (SAED) pattern. (b) HRTEM image of mesoporous α-Fe_2O_3 in which the Fe_2O_3 lattice can be clearly resolved.

To examine the specific surface area and the pore size distribution, N_2 adsorption−desorption isotherm measurements were carried out. The curve shown in Figure 4a depicts a typical H_2-type hysteresis loop, which makes it clear that the distribution of the pore sizes and shapes is heterogeneous.[6] This further confirmed the TEM results shown in Figure 3. The pore size distribution, obtained from the Barrett−Joyner−Halenda (BJH) method, is shown in Figure 4b. The plot shows that the dominant peaks are in the mesoporous range with a wide main peak around 7 nm and a small narrow peak at 15 nm.[38] The two main peaks in pore size distribution suggest that the mesopores are distributed over a wide range of sizes. The surface area estimated from the Brunauer−Emmett−Teller (BET) method is 128 m^2 g^{-1}. The high surface area of the mesoporous structures will be of benefit for improvement of the sensitivity in gas sensors and for increased reversible lithium storage capacity as anode material in lithium ion batteries.

3.2. Magnetic Properties of Mesoporous α-Fe_2O_3. Figure 5 shows temperature dependence of magnetic moment in the applied field of 1 T. For ZFCW regime, the moment increases strongly with temperature up to 50 K. This is followed by a weak decrease of the moment with temperature for temperatures up to 180 K. There is an abrupt increase of magnetic moment with temperature between 180 and 228 K. This steep increase corresponds to Morin transition, a characteristic feature of α-Fe_2O_3.[39] Magnetic moment decreases with temperature above 228 K. Similar features are also obtained for FCC and FCW

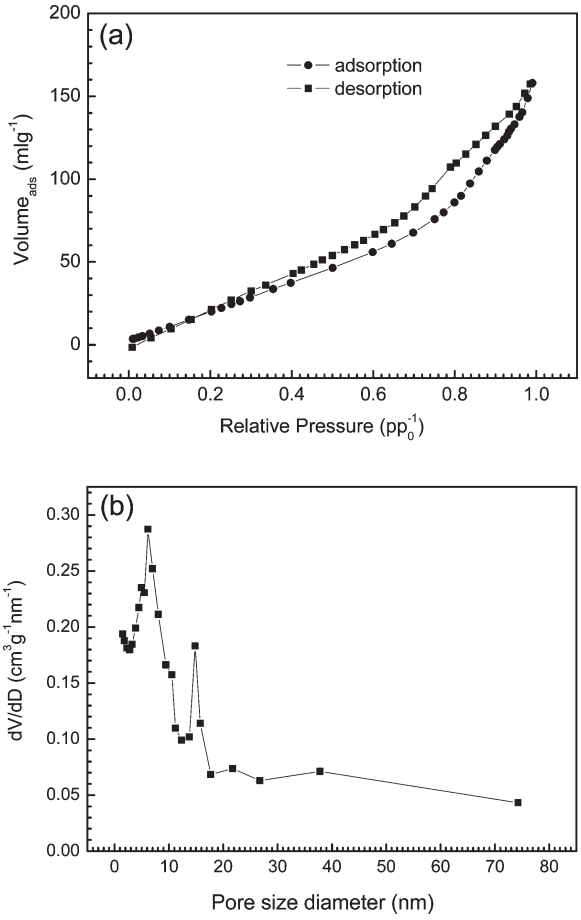

Figure 4. (a) Adsorption−desorption isotherms of mesoporous α-Fe_2O_3 and (b) pore size distribution calculated from the desorption isotherm.

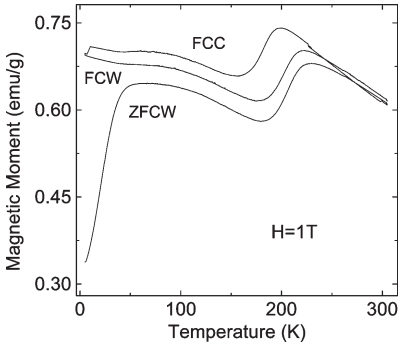

Figure 5. Temperature dependence of magnetic moment of mesoporous α-Fe_2O_3 for zero-field-cooled measurements upon warming (ZFCW), field-cooled measurements upon cooling (FCC), and field-cooled measurements upon warming (FCW).

measurements, however, there is no increase of the moment with temperature for $T < 50$ K. Instead, the magnetic moment slightly decreases with temperature up to 50 K followed by a further decrease with a different rate. There is no overlap of ZFCW, FCC, or FCW branches in any measured temperature range. The Morin transition occurs at lower temperature for the FCW and FCC measurements than for the ZFCW ones. The width of the Morin transition of ∼40 K indicates a wide distribution of the crystal properties in the mesoporous samples.

The Morin transition occurs at Morin temperature T_M because of competition between different anisotropy terms in α-Fe_2O_3 as described by Artman et al.[39] Antiferromagnetically ordered spins in macroscopic α-Fe_2O_3 crystals are oriented along trigonal [111] axis below T_M. The sample has no net magnetic moment at these temperatures. The spins are flipped into the basal (111) plane above T_M and are also antiferromagnetically ordered. However, they are slightly canted out of the perfect antiferromagnetic alignment. This canted component of the spins couples ferromagnetically, which gives rise to a small net magnetic moment of α-Fe_2O_3 above T_M.

The transition between the ferromagnetic (FM) and antiferromagnetic (AFM) state is the first-order magnetic transition. Although the bulk free energy of the AFM and FM states are the same at T_M, there is an energy barrier associated with the transition between the two states. Chow and Keffer showed that surface anisotropies and their interaction with the bulk states have to be considered to explain these transitions.[40] The surface states do not contribute appreciably to the net magnetic moment because they are confined to a thin surface layer. However, they define the way the energy barrier is overcome upon the transition between the two states. In the case of weak surface anisotropy, the transition from AFM to FM state during warming occurs at T_M of the bulk spins. However, FM to AFM transition during cooling occurs at a lower temperature than T_M.[40] For strong surface anisotropy, it is the opposite: FM to AFM transition occurs at bulk T_M upon cooling and AFM to FM transition occurs at a $T > T_M$ upon warming.

Our measurements are consistent with the model of Chow and Keffer.[40] The transitions between AFM and FM states upon warming occur at higher temperatures than upon cooling (Figure 5). The difference between ZFCW and FCW could be associated with irreversibilities of surface states. Magnetic anisotropy is defined by coupling of spins to the crystal lattice order. In the absence of a strong crystal order, magnetic anisotropy decreases. Because surface of our nanoparticles is associated with a crystal disorder that results in unpaired spins, it is reasonable to assume that magnetic anisotropy on the surface is weaker than deeper inside the nanoparticles. According to the model of Chow and Keffer, T_M is then obtained from the transition in ZFCW measurements.

The value of T_M for macroscopic α-Fe_2O_3 is 263 K, and it depends on the crystal size when the crystals are smaller than ∼100 nm. Using the data reported by Zysler et al.,[41] the value of T_M of 209 K for our samples suggests the average crystal size of about 20−40 nm, which is consistent with the result of XRD analysis. These crystallites agglomerate into lumps of a few hundred nanometers in size as observed by TEM and HRTEM analysis. This is similar to the report on α-Fe_2O_3 particles obtained by reaction of 2×10^{-2} M $FeCl_3$ and 3×10^{-4} M NaH_2PO_4.[41]

The transition temperature between AFM and FM states is field-dependent, which was also reported by Qian et al.[42] The transition temperature in our FCC measurements decreases with the field at a rate of 9 K/T from its value of 191 K at 0.01 T. This field dependence of transition temperature points to magnetic irreversibilities associated with ferromagnetic ordering in α-Fe_2O_3 that was not destroyed by warming the sample to 305 K. This is due to existence of the intrinsic ferromagnetic ordering above T_M of Artman-type but is also due to the unpaired spins on the surface of α-Fe_2O_3 crystals. There is also interaction between nanoparticles of agglomerates, which will depend on thermal history due to reorientation of the nanoparticles within the agglomerates.

The other features of the observed temperature dependence of the magnetic moment can be explained in terms of ferromagnetic ordering of unpaired surface spins on the top of the antiferromagnetic moment of the bulk hematite. The magnetic

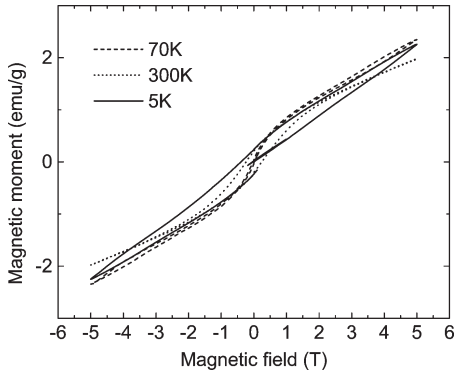

Figure 6. Magnetic hysteresis loops of mesoporous α-Fe_2O_3 measured at different temperatures: 5, 70, and 300 K.

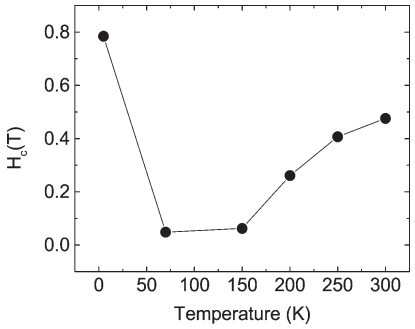

Figure 7. Temperature dependence of the coercive field for mesoporous α-Fe_2O_3.

moment of our sample at 1 T and 200 K is about 0.6 emu/g. Hematite single crystal has magnetic susceptibility at 200 K for parallel and perpendicular direction to the easy axis of about 3×10^{-6} and 18×10^{-6} emu/(g Oe), respectively.[43] This results in a magnetic susceptibility for powder with randomly oriented crystals of 13×10^{-6} emu/(g Oe). Taking into account this antiferromagnetic susceptibility, surface spins contribute 0.47 emu/g to the magnetic moment at 200 K and 1 T (Figure 5). This is substantially more than the additional ∼0.15 emu/g contributed by the Morin transition just above 200 K. The Artman-type magnetic moment in macroscopic hematite crystals is 0.4 emu/g,[43] which is substantially higher than the increase by 0.15 emu/g at the Morin transition for our sample. This is probably because our sample consists of some crystallites smaller than the particular size d_0 at which T_M vanishes if the particle sizes are smaller than d_0. The value of d_0 can be estimated from the report by Zysler at al. to be about 10 nm.[41] The Morin temperature T_M decreases with particle size and strains in the particles.[44] Therefore, particles smaller than d_0 do not undergo Morin transition at the measured temperatures. Instead, these particles have the Artman-type ferromagnetic component at all measured temperatures as shown by Bodker at al.[45] As a result, the increase of the magnetic moment upon Morin transition, normalized to the total sample mass, is smaller than for the samples where all of the particles undergo Morin transition. Therefore, these sub-d_0 particles contribute to the superparamagnetic behavior because of their Artman-type magnetic moment. There are also unpaired surface spins. For particles smaller than d_0, these surface spins will contribute to superparamagnetic behavior because they are coupled to the canted Artman-type bulk magnetic moment at all temperatures. Coupling of the unpaired surface spins to the antiferromagnetic bulk order is also likely to contribute because this coupling is disturbed by the surface disorder for particles of any sizes. Thus, both surface spins and Artman-type magnetic moment of sub-d_0 particles contribute to the magnetic moment of 0.47 emu/g just below 200 K at 1 T. The mesoporous α-Fe_2O_3 seems to be in superparamagnetic state for 50 K < T < 200 K as indicated by magnetic hysteresis loops (Figure 6). The unpaired surface spins and the Artman-type contribution of sub-d_0 particles are responsible for this superparamagnetic state. There is a strong increase of magnetic irreversibility for T < 50 K (Figure 5) indicating yet another magnetic transition. A similar effect was also reported by Jiao et al.[28]

Most likely this can be ascribed to the blocking transition at 50 K, where superparamagnetic spins freeze-in upon cooling and give an almost constant magnetic moment. This moment is zero if cooling is in zero field. With warming up in ZFCW measurements, the magnetic moment rises with temperature as an increasing number of spins gets unfrozen by thermal excitation and gets aligned in the direction of the field. Finally, above blocking temperature, superparamagnetic system occurs. Measurements in Figure 5 are consistent with this picture as ZFCW magnetic moment increases from a low value at 5 K up to its maximum value at the blocking temperature of 50 K. Above 50 K, the sample is in superparamagnetic state for H = 1 T showing a very small coercive field and S-shaped hysteresis loops typical of superparamagnetic particles (Figures 6 and 7). This transition temperature is field-dependent. It increases from 53 K at 1 T to 96 K at 0.01 T. This is also consistent with the picture of unfreezing spins as the temperature increases in ZFCW measurements. A higher magnetic field exerts larger force on misaligned spins, and a lower energy of thermal excitation is required to align them in the direction of the field. With the lower field, higher thermal excitations are required for the same effect.

The ZFCW, FCC, and FCW curves do not overlap above 200 K. The reason for this could be the irreversibilities associated with the ordering of surface spins that are still not suppressed at these temperatures as well as Artman-type ferromagnetic order above T_M. However, there is also a possibility of magnetic nanoparticles rotating upon thermal cycling within the agglomerates in a different way for FCC, FCW, and ZFCW measurements. This changes the interaction between the nanoparticles and results in additional irreversibilities that depend on the way the measurements are performed.[41] A good indication for this effect is that the magnetic moment for T > 200 K in Figure 5 measured upon warming decreases with temperature with the same rate for ZCFW and FCW measurements. However, magnetic moment measured upon cooling (FCC) in the same temperature range and the same field decreases with temperature at a higher rate.

The coercive field of our nanoparticles at room temperature is much larger than for bulk crystals (Figure 7).The coercive field can be strongly affected by distribution of sizes of nanoparticles as well as by their interaction within the agglomerates. H_c of similar magnitude to our samples was obtained for hematite nanoparticles that were densely packed into agglomerates. Loosely packed nanoparticles gave ∼10 times lower H_c.[42] This supports our argument on the importance of nanoparticle interaction to their magnetic properties.

Magnetic hysteresis loops are in agreement with the above description (Figure 5). The hysteresis loop measured at 5 K strongly differs from the ones measured above 50 K. It has much larger coercive field, H_c, than the hysteresis loops measured between 50 and 200 K (Figures 6 and 7). The hysteresis loops between 50 and 200 K are distinctly S-shaped with vanishingly low coercive field as expected for superparamagnetic particles. H_c starts increasing with the onset of Artman-type ferromag-

netism for nanoparticles larger than d_0 at ~200 K (Figure 7). Superparamagnetic behavior seems to be suppressed for $T >$ 200 K because of an additional magnetic moment arising from Artman-type of ordering. The interaction between the nanoparticles within the mesoporous structures probably plays an important role in these processes even though its magnitude and the exact mechanisms are still unknown. The increase of H_c and the appearance of ferromagnetic order at temperatures higher than the blocking temperature may sound confusing. However, there are two families of spins contributing to the measured magnetic moment: unpaired surface spins and bulk spins due to Artman-type transition. When both of them are ordered ferromagnetically, the net magnetic moment may be large enough to give the observed ferromagnetic behavior. Nanoparticle agglomeration probably also plays a role here through magnetic coupling of nanoparticles.

Therefore, surface spins and Artman-type magnetic moment of sub-d_0 nanoparticles dominate the magnetic behavior of mesoporous α-Fe_2O_3 below 200 K. There is evidence for superparamagnetic behavior of this system with blocking temperature around 50 K at 1 T. Morin transition of particles larger than d_0 occurs at 200 K giving additional ferromagnetic contribution above 200 K. The magnetic moment of the surface spins and sub-d_0 particles with Artman-type ordering is about 3 times higher than the one due to Morin transition of particles larger than d_0 at 200 K and 1 T. There seems to be an effect of orientation of the nanoparticles within the mesoporous structures on the net magnetic moment. As this orientation changes with field and temperature, so does the magnetic interaction between the nanoparticles giving a magnetic moment that depends on history of thermal cycling in magnetic field.

3.3. Gas-Sensing Performance. The gas-sensing performance of the as-prepared mesoporous α-Fe_2O_3 was investigated toward a variety of flammable, toxic, and corrosive gases such as ethanol, acetone, gasoline, heptane, formaldehyde, acetic acid, 1-butanol, and 2-propanol. Figure 8a displays the real-time sensing response characteristics toward ethanol of a sensor based on the as-prepared mesoporous α-Fe_2O_3 at a working temperature of 150 °C and 30% relative humidity (RH). It can be seen that the value of the output voltage increased abruptly after the injection of ethanol and recovered its initial value after release of the gas. The response and recovery times (defined as the time required to reach 90% of the final equilibrium value) of the as-prepared mesoporous α-Fe_2O_3 based sensor were only 1−3 s each indicating their rapid response and good reversibility. From Ohm's law, the electric resistance of the sensor underwent a decrease (increase) when the ethanol was injected (released), which is the typical sensor behavior of n-type semiconductor sensors. In the ambient environment, n-type α-Fe_2O_3 is expected to adsorb both oxygen and moisture. The adsorbed O^{2-} and OH^- groups trap electrons from the conduction band of the α-Fe_2O_3 nanocrystals and increase the resistance of the sensor. When the sensor is exposed to ethanol, the test gas molecules are chemiadsorbed at the active sites on the surface of the as-prepared mesoporous α-Fe_2O_3. These molecules will be oxidized by the adsorbed oxygen and the lattice oxygen (O^{2-}) of α-Fe_2O_3 at the sensor working temperature (150 °C). In this process, electrons will be transferred to the surface of the as-prepared mesoporous α-Fe_2O_3 to lower the number of trapped electrons inducing a decrease in the resistance.[10] The magnitude of the response for a sensor based on the as-prepared mesoporous α-Fe_2O_3 improved dramatically with increasing the concentration of the ethanol from 5 ppm to 1000 ppm suggesting that the as-prepared mesoporous α-Fe_2O_3 has good sensitivity toward

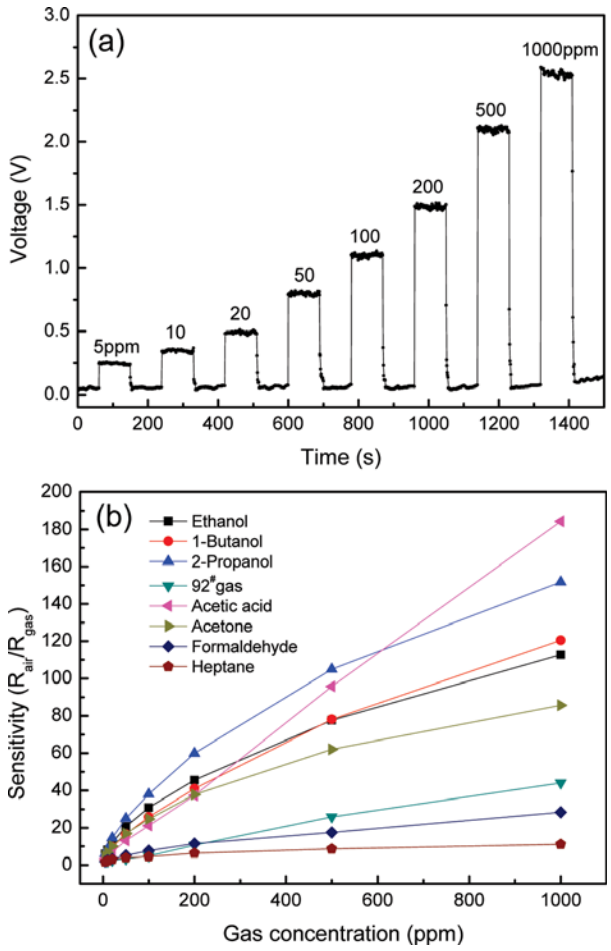

Figure 8. (a) Real-time ethanol sensing characterization of sensors based on the as-prepared mesoporous α-Fe_2O_3. (b) Sensitivity of the sensors based on as-prepared mesoporous α-Fe_2O_3 toward different gases or vapors.

ethanol. After eight cycles between the ethanol and fresh air, the output voltages could still recover to their initial states indicating excellent reversibility. Figure 8b presents the sensitivity of a sensor based on the as-prepared mesoporous α-Fe_2O_3 toward a variety of gases at different concentrations. The gas sensitivity (S) is defined as the ratio of the stationary electrical resistance of the sensor in air (R_{air}) to its resistance in the test gas (R_{gas}), that is, $S = R_{air}/R_{gas}$. The as-prepared mesoporous α-Fe_2O_3 exhibited a very impressive sensitivity toward ethanol at high concentration (1000 ppm), which is better than the performance of its nanosphere and nanowire counterparts as we previously reported.[9,10] The improvement of the sensing performance of the as-prepared mesoporous α-Fe_2O_3 may be attributed to the mesoporous structure. The highly porous structure leads to high specific surface area, which is measured to be 128 m^2/g resulting in more active sites for gas chemisorption. The abundant open pores distributed in the three-dimensional space can facilitate the diffusion of the test gas and can improve the kinetics of both the reaction of the test gas with surface adsorbed oxygen and the replacement of the latter from the gas phase. From Figure 8b, we can also note that the as-prepared mesoporous α-Fe_2O_3 sensor also has high sensitivity toward some other flammable and explosive gases such as 92# gasoline, 2-propanol, 1-butanol, heptane, and acetone. However, the sensor could barely detect heptane even at high concentration (e.g., 1000 ppm). For application in air quality monitoring, we also investigated the sensing performance of the as-prepared mesoporous α-Fe_2O_3 to some toxic, corrosive,

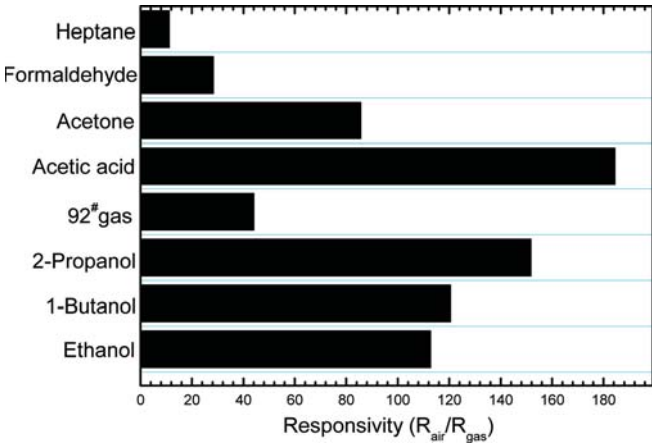

Figure 9. Sensitivity of the sensors based on as-prepared mesoporous α-Fe_2O_3 toward different gases or vapors at a concentration of 1000 ppm.

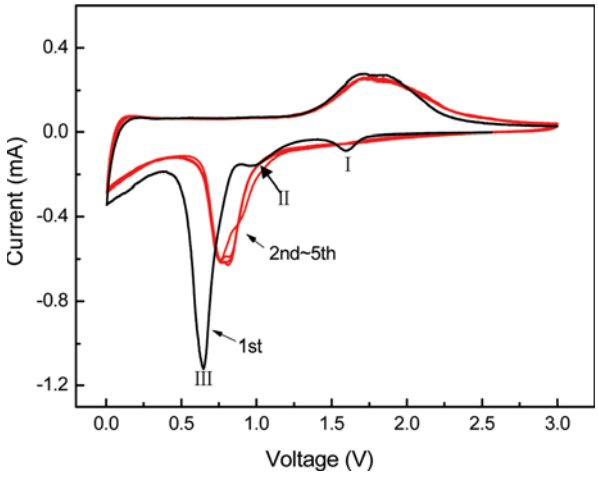

Figure 10. Cyclic voltammentry (CV) curves of the cell with anode prepared from mesoporous α-Fe_2O_3 (scanning rate: 0.1 mVs^{-1} in the range of 0.005−3.0 V).

and irritating gases, such as formaldehyde and acetic acid. It is interesting that the as-prepared mesoporous α-Fe_2O_3 displayed the highest responsiveness to acetic acid (Figure 8b) with S reaching as high as $S = 185$ in the presence of 1000 ppm of acetic acid vapor. This ultrahigh sensitivity may be caused by the strong chemisorption of acetic acid on the surface of the as-prepared mesoporous α-Fe_2O_3 owing to the strong coordination of carboxyl to Fe^{3+}. For comparison, Figure 9 presents a bar graph of the sensitivity of the mesoporous α-Fe_2O_3 sensor toward eight types of gases or vapors at a concentration of 1000 ppm. We can clearly identify that the as-prepared mesoporous α-Fe_2O_3 showed the highest sensitivity and selectivity toward acetic acid as opposed to any other gas. On the other hand, the as-prepared mesoporous α-Fe_2O_3 can selectively detect alcohol in the presence of other flammable and explosive gases, such as acetone, 92# gasoline, and heptane. However, the sensor could barely detect heptane indicating that the as-prepared mesoporous α-Fe_2O_3 based sensor has a degree of selectivity to different gases.

3.4. Electrochemical Performance in Lithium Ion Battery. The electrochemical behavior of the electrode made from the as-prepared mesoporous α-Fe_2O_3 was evaluated by cyclic voltammetry (CV) and galvanostatic charge/discharge cycling. Figure 10 shows the CV curves of the mesoporous α-Fe_2O_3 anode. During the cathodic polarization in the first cycle, a spiky peak was observed at 0.65 V with two small peaks appearing at 1.0 and 1.6 V indicating the following three lithiation steps[7,8]

$$\alpha\text{-}Fe_2O_3 + xLi^+ + xe^- \rightarrow \alpha\text{-}Li_xFe_2O_3 \quad (2)$$

$$\alpha\text{-}Li_xFe_2O_3 + (2 - x)Li^+ + (2 - x)e^- \rightarrow Li_2Fe_2O_3(\text{cubic}) \quad (3)$$

$$Li_2Fe_2O_3(\text{cubic}) + 4Li^+ + 4e^- \leftrightarrow 2Fe^0 + 3Li_2O \quad (4)$$

$$\alpha\text{-}Fe_2O_3 + 6Li^+ + 6e^- \rightarrow 2Fe^0 + 3Li_2O$$

At the initial stage of lithium intercalation (peak I), a small amount of lithium can be inserted into the crystal structure of the as-prepared mesoporous α-Fe_2O_3 without change in the structure. In the next step of lithium intercalation (peak II), the hexagonal α-$Li_xFe_2O_3$ is transformed to cubic $Li_2Fe_2O_3$. The spiky peak (peak III) corresponds to the complete reduction of iron from Fe^{2+} to Fe^{0+} and the decomposition of electrolyte. On the other hand, in the anodic polarization process, two broad overlapping peaks were recorded at about 1.7 and 1.85 V corresponding to the oxidation of Fe^0 to Fe^{2+} and further oxidization to Fe^{3+}.[46] The curves of the subsequent cycles are significantly different from that of the first cycle as only one cathodic peak appears at about 0.8 V with decreased peak intensity, while the anodic polarization only showed one broad peak with a little decrease in peak intensity. The difference between the first and the second cathodic curves is due to an irreversible phase transformation during the process of lithium insertion and extraction in the initial cycle. After the first discharge process, α-Fe_2O_3 was completely reduced to iron nanoparticles and was dispersed in a Li_2O matrix.[47] The disappearance of the peaks at 1.6 V and 1.0 V from the second cathodic process indicates that the lithium insertion reaction and phase transformation from hexagonal α-$Li_xFe_2O_3$ to cubic $Li_2Fe_2O_3$ are irreversible.[46] The decrease of the redox peak intensity implies that the capacity is decreased during cycling. After the second cycle, the CV curves are very stable for the mesoporous α-Fe_2O_3 electrode indicating enhanced stability during the lithiation and delithiation processes.

The charge−discharge curves of the mesoporous α-Fe_2O_3 electrode during the first and second cycles are shown in Figure 11a, and these are typical charge−discharge curves for transition metal anode materials.[47] For the discharge curve in the first cycle, the voltage initially decreased quickly to approximately 1.6 V followed by a weak slope corresponding to the initial lithium insertion into the α-Fe_2O_3 without any change in the structure. There is also a wide slope located at 1.2−0.85 V, where there is a phase transformation from the hexagonal α-$Li_xFe_2O_3$ to the cubic $Li_2Fe_2O_3$. An obvious plateau was observed at 0.85 V indicating the complete reduction of iron from Fe^{2+} to Fe^{0+}. This electrochemical behavior is consistent with the results of the CV measurement. The capacity obtained above 0.8 V is 940 mAh g^{-1} (5.6 mol of Li per mole of α-Fe_2O_3), which is very close to the theoretical capacity of 1007 mAh g^{-1} (6 mol of Li per mole of α-Fe_2O_3). After discharging the voltage to 0.01 V, the total specific capacity of the as-prepared mesoporous α-Fe_2O_3 is 1730 mAh g^{-1} corresponding to 10.3 mol of Li per mole of α-Fe_2O_3, which is much higher than the theoretical capacity. The large excess capacity could

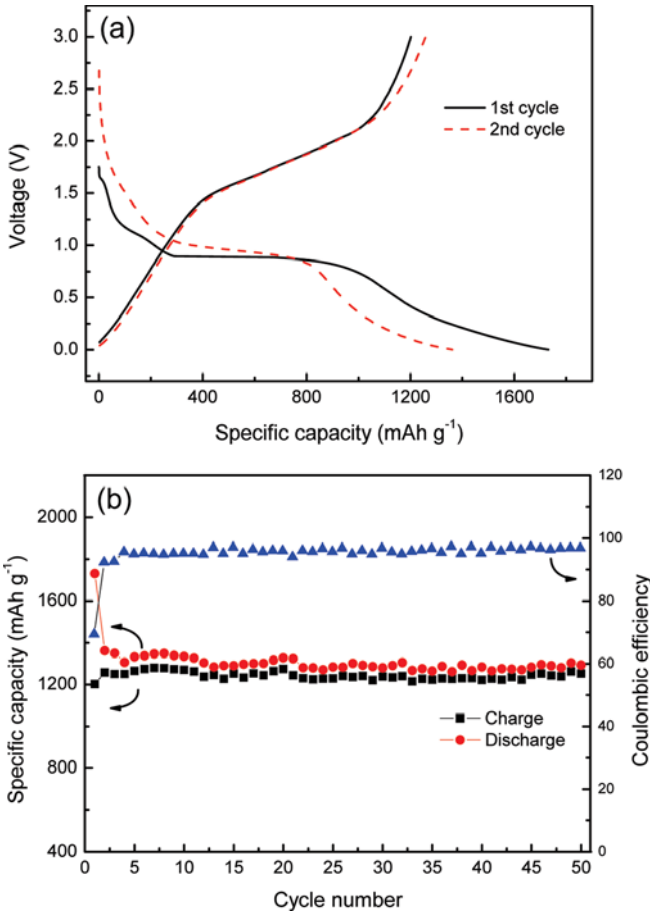

Figure 11. Charge−discharge performance of the electrode made from the as-prepared mesoporous α-Fe_2O_3: (a) the voltage profiles of the first two cycles, (b) cycling performance.

be ascribed to the decomposition of the electrolyte at low voltage (generally below 0.8 V vs Li^+/Li) to form a solid electrolyte interphase (SEI) layer and further lithium storage via interfacial charging at metal/Li_2O interface.[48−51] It has been demonstrated in previous reports that the morphology plays a significant role in the discharge performance.[12,52] The materials that have small particles with high surface area always yield high discharge capacities indicating that high surface area can enhance the interfacial charge storage. During the second cycle, the discharge curve only shows a slope at 1.0−0.8 V, and the capacity is reduced to 1360 mAh g^{-1}. Usually, the slope behavior during the discharge process of metal oxide anode materials is considered to relate to the irreversible formation of a nanocomposite of crystalline grains of metals and amorphous Li_2O matrix.[48,53] For the charge curves of the first and second cycles, no obvious plateau can be observed and the charge capacities are 1200 mAh g^{-1} and 1250 mAh g^{-1}, respectively, corresponding to the oxidation of Fe^0 to Fe^{2+}, with part of the Fe further oxidized to Fe^{3+}, along with some contribution from the reversible surface layer formed during the discharge process. The cycling performance of mesoporous α-Fe_2O_3 electrode is shown in Figure 11b, which demonstrates an excellent cycling performance. After 50 cycles at a current rate of 200 mA g^{-1} (0.2C), the specific discharge capacity is 1293 mAh g^{-1}, which is about 95% of the second cycle discharge capacity and represents a 0.1% capacity drop per cycle apart from the first cycle. The excellent capacity retention should be related to the mesoporous structure of the materials, which can accommodate the volume change of the Li^+ insertion/extraction during the

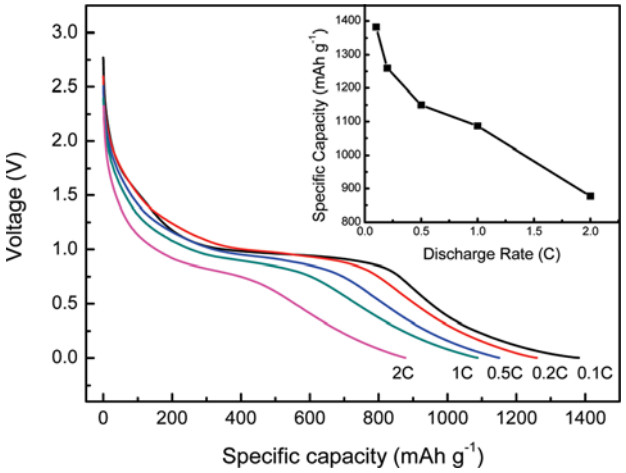

Figure 12. Discharge voltage profiles of the electrode made of as-prepared mesoporous α-Fe_2O_3 at different current densities. The insert is the discharge specific capacity at different C-rates.

charge−discharge processes and which can prevent the active materials from falling off the current collector.[49,54]

We also investigated the electrochemical performance of mesoporous α-Fe_2O_3 electrodes at different current densities (as shown in Figure 12). Even at the 2C (2000 mA g^{-1}) rate, we achieved a specific lithium storage capacity of 870 mAh g^{-1}, which is much higher than the theoretical capacity of graphite (372 mAh g^{-1}). The mesoporous structure with high surface area provides high surface contact with the electrolyte and decreases the current density per unit area. To our knowledge, this is the best performance compared with the previously reported electrochemical performance for α-Fe_2O_3 material.[2,11,12,14,17,53] The excellent cycling stability and high rate specific capacity of the as-prepared mesoporous α-Fe_2O_3 indicate its attractive potential for use as an anode material in lithium ion batteries.

4. Conclusions

Herein, we used a soft template synthesis method to successfully prepare mesoporous α-Fe_2O_3. The as-prepared material shows a highly porous structure with a large surface area of 128 m^2 g^{-1}. Magnetic property measurement shows that surface spins dominate the magnetic behavior of mesoporous α-Fe_2O_3 material. The contribution of the surface spins to magnetic moment at 200 K is about 3 times higher than the one due to Morin transition at $H = 1$ T. Mesoporous α-Fe_2O_3 materials exhibit superparamagnetic behavior because of small particle size with blocking temperature at 1 T field of 50 K. The Morin transition at ∼200 K is also associated with the surface spins. In the gas-sensing experiments, the as-prepared mesoporous α-Fe_2O_3 exhibits high sensitivities toward acetic acid and alcohol indicating its potential application in monitoring corrosive and flammable gases. For use as anode materials in lithium ion batteries, the as-prepared mesoporous α-Fe_2O_3 shows a high discharge specific capacity of 1730 mAh g^{-1} for the first cycle and 1293 mAh g^{-1} after 50 cycles. The good cycling stability and high rate specific capacity indicate its potential for application in the lithium ion battery industry.

Acknowledgment. We gratefully acknowledge financial support from Bezel (Changzhou) New Energy Science & Technology Co., Ltd., Daejung Energy Materials Co., Ltd., Korea, and an ARC Discovery project (DP07729999) from the Australian Research Council.

Supporting Information Available: Schematic diagram of the gas sensor system and TEM images of mesoporous α-Fe_2O_3. This material is available free of charge via the Internet at http://pubs.acs.org.

References and Notes

(1) Jain, G.; Balasubramanian, M.; Xu, J. J. *Chem. Mater.* **2006**, *18*, 423.
(2) Wu, C. Z.; Yin, P.; Zhu, X.; OuYang, C. Z.; Xie, Y. *J. Phys. Chem. B* **2006**, *110*, 17806.
(3) Gou, X. L.; Wang, G. X.; Kong, X. Y.; Wexler, D.; Horvat, J.; Yang, J.; Park, J. *Chem.—Eur. J.* **2008**, *14*, 5996.
(4) Hermanek, M.; Zboril, R.; Medrik, N.; Pechousek, J.; Gregor, C. *J. Am. Chem. Soc.* **2007**, *129*, 10929.
(5) Feldmann, C. *Adv. Mater.* **2001**, *13*, 1301.
(6) Srivastava, D. N.; Perkas, N.; Gedanken, A.; Felner, I. *J. Phys. Chem. B* **2002**, *106*, 1878.
(7) Larcher, D.; Masquelier, C.; Bonnin, D.; Chabre, Y.; Masson, V.; Leriche, J. B.; Tarascon, J. M. *J. Electrochem. Soc.* **2003**, *150*, A133.
(8) Larcher, D.; Bonnin, D.; Cortes, R.; Rivals, I.; Personnaz, L.; Tarascon, J. M. *J. Electrochem. Soc.* **2003**, *150*, A1643.
(9) Gou, X. L.; Wang, G. X.; Park, J.; Liu, H.; Yang, J. *Nanotechnology* **2008**, *19*, 125606.
(10) Wang, G. X.; Gou, X. L.; Horvat, J.; Park, J. *J. Phys. Chem. C* **2008**, *112*, 15220.
(11) Chen, J.; Xu, L. N.; Li, W. Y.; Gou, X. L. *Adv. Mater.* **2005**, *17*, 582.
(12) Reddy, M. V.; Yu, T.; Sow, C. H.; Shen, Z. X.; Lim, C. T.; Rao, G. V. S.; Chowdari, B. V. R. *Adv. Funct. Mater.* **2007**, *17*, 2792.
(13) Tahir, A. A.; Wijayantha, K. G. U.; Saremi-Yarahmadi, S.; Mazhar, M.; McKee, V. *Chem. Mater.* **2009**, *21*, 3763.
(14) Wu, Z. C.; Yu, K.; Zhang, S. D.; Xie, Y. *J. Phys. Chem. C* **2008**, *112*, 11307.
(15) Woo, K.; Lee, H. J.; Ahn, J. P.; Park, Y. S. *Adv. Mater.* **2003**, *15*, 1761.
(16) Dong, W. T.; Zhu, C. S. *J. Mater. Chem.* **2002**, *12*, 1676.
(17) Wang, L.; Xu, H. W.; Chen, P. C.; Zhang, D. W.; Ding, C. X.; Chen, C. H. *J. Power Sources* **2009**, *193*, 846.
(18) Zeng, S. Y.; Tang, K. B.; Li, T. W.; Liang, Z. H.; Wang, D.; Wang, Y. K.; Qi, Y. X.; Zhou, W. W. *J. Phys. Chem. C* **2008**, *112*, 4836.
(19) Lian, J. B.; Duan, X. C.; Ma, J. M.; Peng, P.; Kim, T. I.; Zheng, W. J. *ACS Nano* **2009**, *3*, 3749.
(20) Cheng, F.; Tao, Z.; Liang, J.; Chen, J. *Chem. Mater.* **2008**, *20*, 667.
(21) Liu, J. P.; Li, Y. Y.; Fan, H. J.; Zhu, Z. H.; Jiang, J.; Ding, R. M.; Hu, Y. Y.; Huang, X. T. *Chem. Mater.* **2010**, *22*, 212.
(22) Kresge, C. T.; Leonowicz, M. E.; Roth, W. J.; Vartuli, J. C.; Beck, J. S. *Nature* **1992**, *359*, 710.
(23) He, X.; Antonelli, D. *Angew. Chem., Int. Ed.* **2002**, *41*, 214.
(24) Jiao, F.; Harrison, A.; Hill, A. H.; Bruce, P. G. *Adv. Mater.* **2007**, *19*, 4063.
(25) Yu, C. C.; Dong, X. P.; Guo, L. M.; Li, J. T.; Qin, F.; Zhang, L. X.; Shi, J. L.; Yan, D. S. *J. Phys. Chem. C* **2008**, *112*, 13378.
(26) Jiao, F.; Bruce, P. G. *Adv. Mater.* **2007**, *19*, 657.
(27) Shaju, K. M.; Jiao, F.; Debart, A.; Bruce, P. G. *Phys. Chem. Chem. Phys.* **2007**, *9*, 1837.
(28) Jiao, F.; Harrison, A.; Jumas, J. C.; Chadwick, A. V.; Kockelmann, W.; Bruce, P. G. *J. Am. Chem. Soc.* **2006**, *128*, 5468.
(29) Wang, K. X.; Wei, M. D.; Morris, M. A.; Zhou, H. S.; Holmes, J. D. *Adv. Mater.* **2007**, *19*, 3016.
(30) Liu, P.; Lee, S. H.; Tracy, C. E.; Yan, Y. F.; Turner, J. A. *Adv. Mater.* **2002**, *14*, 27.
(31) Yang, P. D.; Zhao, D. Y.; Margolese, D. I.; Chmelka, B. F.; Stucky, G. D. *Nature* **1998**, *396*, 152.
(32) Yang, P. D.; Zhao, D. Y.; Margolese, D. I.; Chmelka, B. F.; Stucky, G. D. *Chem. Mater.* **1999**, *11*, 2813.
(33) Laetsch, T.; Downs, R. T. 19th General Meeting of the International Mineralogical Association, Kobe, Japan.
(34) Kim, C. H.; Chun, H. J.; Kim, D. S.; Kim, S. Y.; Park, J.; Moon, J. Y.; Lee, G.; Yoon, J.; Jo, Y.; Jung, M. H.; Jung, S. I.; Lee, C. J. *Appl. Phys. Lett.* **2006**, *89*, 223103.
(35) Bersani, D.; Lottici, P. P.; Montenero, A. *J. Raman Spectrosc.* **1999**, *30*, 355.
(36) Akl, A. A. *Appl. Surf. Sci.* **2004**, *233*, 307.
(37) Vayssieres, L.; Sathe, C.; Butorin, S. M.; Shuh, D. K.; Nordgren, J.; Guo, J. H. *Adv. Mater.* **2005**, *17*, 2320.
(38) Corma, A. *Chem. Rev.* **1997**, *97*, 2373.
(39) Artman, J. O.; Murphy, J. C.; Foner, S. *Phys. Rev.* **1965**, *138*, A912.
(40) Chow, H.; Keffer, F. *Phys. Rev. B* **1974**, *10*, 243.
(41) Zysler, R. D.; et al. *Phys. Rev. B* **2003**, *68*, 212408.
(42) Qian, H.; Han, G.; Lin, G.; Xu, R. *AIChE J.* **2008**, *8*, 51.
(43) Flanders, P. J.; Remeika, J. P. *Philos. Mag.* **1965**, *11*, 1271.
(44) Muench, G. J.; Arajs, S.; Matijević, E. *Phys. Status Solidi A* **1985**, *92*, 187.
(45) Bødker, F.; Hansen, M. F.; Koch, C. B.; Lefmann, K.; Mørup, S. *Phys. Rev. B* **2000**, *61*, 6826.
(46) Morales, J.; Sanchez, L.; Martin, F.; Berry, F.; Ren, X. L. *J. Electrochem. Soc.* **2005**, *152*, A1748.
(47) Poizot, P.; Laruelle, S.; Grugeon, S.; Dupont, L.; Tarascon, J. M. *Nature* **2000**, *407*, 496.
(48) Jamnik, J.; Maier, J. *Phys. Chem. Chem. Phys.* **2003**, *5*, 5215.
(49) Maier, J. *Nature* **2005**, *4*, 805.
(50) Grugeon, S.; Laruelle, S.; Dupont, L.; Tarascon, J. M. *Solid State Sci.* **2003**, *5*, 895.
(51) Balaya, P.; Li, H.; Kienle, L.; Maier, J. *Adv. Funct. Mater.* **2003**, *13*, 621.
(52) Jiao, F.; Bao, J. L.; Bruce, P. G. *Electrochem. Solid-State Lett.* **2007**, *10*, A264.
(53) Wu, X. L.; Guo, Y. G.; Wan, L. J.; Hu, C. W. *J. Phys. Chem. C* **2008**, *112*, 16824.
(54) Hu, Y. S.; Kienle, L.; Guo, Y. G.; Maier, J. *Adv. Mater.* **2006**, *18*, 1421.

JP102286E